

Magnetic Petrology of Unzen Volcano, Japan: Implications for Lava Dome Oxidation Processes

Takeshi SAITO*, Naoto ISHIKAWA*, and Hiroki KAMATA*

* Graduate school of Human and Environmental Studies, Kyoto University

Synopsis

In order to understand the oxidation state in lava dome, magnetic petrological analyses were carried out on lava samples from the lava domes and block-and-ash-flow deposits of the 1990-1995 eruption of Unzen volcano, Japan. Samples from the surface of actual lava dome were highly oxidized, while those from the inner part were unoxidized. Samples from endogenous dome showed as almost the same oxidation states and processes as those from exogenous dome. This suggested that the different oxidation state is due to the difference of position of the samples in the lava dome rather than the difference of the growth style.

Keywords: Unzen volcano, lava dome, iron-titanium oxide, magnetic petrology, oxidation state

1. Introduction

Non-explosive silicic volcanism has recently attracted many researchers' interests, although explosive volcanism has long been one of the main themes of volcanology (e.g. Newhall and Melson, 1983). Explosive silicic eruptions at Mt. Pelée in 1902 produced nuées ardentes that killed about 28,000 people (La Croix, 1904). On the other hand, non-explosive silicic volcanism is characterized by relatively quiet effusion of lava flows or domes and was recognized to be not very dangerous in the past. However, recent eruptions resulted in changing the recognition. Lava dome effused on steep slope, such as the summit, frequently collapsed and generated small pyroclastic flows (block-and-ash flows) at the 1930 eruption of Merapi volcano, Indonesia (Neumann van Padang, 1933), the 1967 eruption of Santiaguito volcano, Guatemala (Stoiber and Rose, 1969) and the 1990-1995 eruption of Unzen volcano, Japan (Nakada et al., 1999). These eruptions have made us realize that even non-explosive effusion of lava dome result in generation of block-and-ash flows, which can have devastating

human behavior.

Therefore many studies with lava dome eruptions have been carried out in recent years. Particularly, in Japan, the 1990-1995 eruption of Unzen volcano has been studied from various perspectives. Most studies aimed to understand physical and chemical phenomena in magma reservoir or conduit. This is because the processes, which trigger the eruption and rule the eruption style, occur within there. In lava dome eruption, the effusion of lava is just the beginning. Block-and-ash flows, which are the most dangerous during the eruption, are generated from the collapse of effused lava. To clarify the physical and chemical phenomena in the lava dome are crucially important in order to understand the generation mechanisms of block-and-ash flows and to mitigate volcanic hazards.

However, the quantitative understandings of generation mechanisms of block-and-ash flows have not advanced yet, although some models were proposed on the basis of visual observations of the lava dome just before generating a block-and-ash flow (Sato et al., 1992; Nakada and Fujii, 1993; Ui et al., 1999). This is not only

because steep topography of lava domes prevents us from surveying and sampling at will but also because silicate minerals, which most petrologists use, do not record the conditions in the dome.

Iron-titanium oxide minerals are very useful for studying lava domes. They are oxidized in such circumstances as lava dome and transformed into composite multiphase grains whose phases have distinct chemical compositions. In addition, two solid solution series, titanomagnetite ($\text{Fe}_{3-x}\text{Ti}_x\text{O}_4$) and titanohematite ($\text{Fe}_{2-y}\text{Ti}_y\text{O}_3$), show magnetic properties and acquire thermoremanent magnetization during cooling from above the Curie temperature or Néel temperature, although the pseudobrookite series ($\text{Fe}_{2-z}\text{Ti}_{1+z}\text{O}_5$) are all paramagnetic. Their magnetic properties depend on compositions, grain sizes and amount of oxide minerals. Therefore, if we identify iron-titanium oxides and determine their properties, we can estimate the oxidation process of iron-titanium oxides during cooling in the lava dome. Such a method of study has been recently graced with a formal name "*magnetic petrology*" (Wasilewski and Warner, 1988) and was introduced by Frost (1991).

However, few studies from such a point of view have been carried out. Numerous studies have adopted iron-titanium oxides as geothermobarometers in order to

estimate the equilibrium state achieved in the magma reservoir or conduit. Recently, Saito et al. (2004) performed magnetic petrological analyses on rock samples from block-and-ash-flow deposits in Yufu volcano, Japan. They quantitatively clarified oxidation states of samples and deuteric oxidation processes which are suggested to have occurred in the lava dome. However, primary data about oxidation in the lava dome are not available yet.

The 1990-1995 eruption of Unzen volcano was monitored and investigated in detail (e.g. Nakada et al., 1999). The growth of lava domes and the generation of block-and-ash flows were recorded. Therefore quantitative study with physical and chemical phenomena in the lava dome is possible. In this work, we carried out magnetic petrological analyses on samples from the lava dome and block-and-ash-flow deposits of the 1990-1995 eruption in order to examine the oxidation state and process in the lava dome.

2. Geological setting

Unzen volcano is one of the most active volcanoes in the Shimabara Peninsula of Kyushu, Japan (Fig. 1). It is located in a volcanotectonic depression, the Unzen

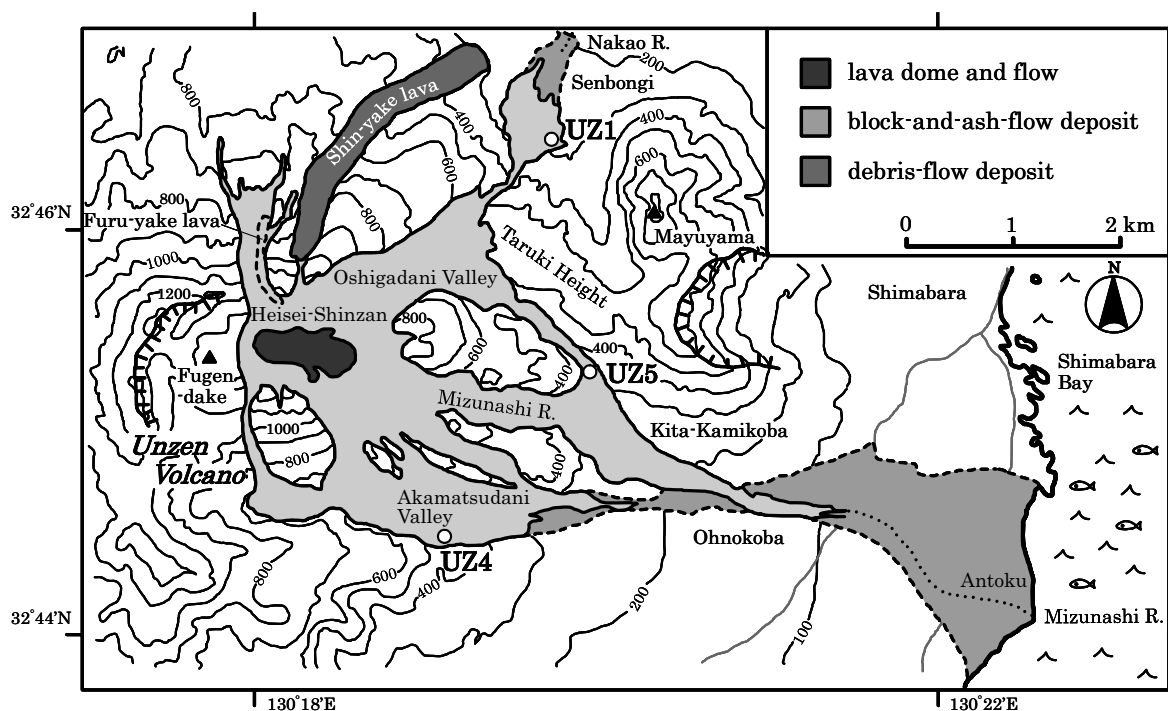


Fig. 1 Simplified geologic map of Unzen volcano after Ui et al. (1999). Sampling locations (UZ1, 4, and 5) are shown.

graben (Ohta, 1973), about 70 km behind the volcanic front of the Southwest Japan Arc. The Unzen graben is the western part of the Beppu-Shimabara Graben, in which many volcanoes are concentrated (Matsumoto, 1993). Unzen is a composite volcano of thick andesite-dacite lavas and pyroclastic materials, covering an area of at least 400 km². Its activity is characterized by non-explosive effusions of lava flows and domes and by block-and-ash flows of dome collapse origin.

Unzen volcano started its activity about half million years ago and the older edifice was constructed between 300 and 200 ka (Hoshizumi et al., 1999). The younger activity started at ca.100 ka and Fugen-dake volcano started its activity about 20 ka. In historic times, Fugen-dake effused an andesite lava flow (Furu-yake) in 1663 and a dacite lava flow (Shin-yake) in 1792. In the 1792 eruption, Mayuyama volcano, located between Fugen-dake and Shimabara city, collapsed by earthquakes and a large debris avalanche was generated. The most recent activity is the 1990-1995 eruption, which is characterized by the effusions of thirteen lava lobes and the generations of abundant block-and-ash flows of dome collapse origin (Nakada et al., 1999).

2.1 Summary of the 1990-1995 eruption

Following 198 years dormancy, Unzen volcano began erupting on 17 November 1990 without preceding explosive eruptions (e.g. Nakada et al., 1999; Miyabuchi, 1999; Nakada, 2000). Unzen effused dacite lava for about four years. Thirteen lava lobes were formed and their partial collapse generated about 9500 block-and-ash flows until 25 May 1995.

At first, phreatic and phreatomagmatic eruptions intermittently occurred at summit vents of Fugen-dake volcano until early May 1991. On 20 May 1991, the first lava dome (lobe 1) appeared in a summit crater and grew exogenously. The first block-and-ash flow occurred and descended along the Mizunashi River on the eastern flank on 24 May 1991. On the afternoon of 3 June 1991, the eastern half of lobe 1 collapsed and relatively large block-and-ash flows occurred. The associated ash cloud surge reached the Kita-Kamikoba area and swept 43 people away in the evacuated zone. On 30 June 1991, rainstorms triggered off the large debris flows along the Mizunashi River. The debris flow devastated the Antoku District and reached Shimabara Bay. The debris flow, triggered by heavy rainfall or typhoons, occurred repeatedly along the lower reach of the Mizunashi River and

damaged more buildings than block-and-ash flows did.

On 15 September 1991, the largest block-and-ash flow in this eruption was generated from lobe 3 and descended along the Oshigadani Valley on the north-eastern flank, reaching the Mizunashi River. An ash-cloud surge, detached from the main flow, swept the Kita-Kamikoba area and reached the Ohnokoba District (Fujii and Nakada, 1999). In February 1992, block-and-ash flows started descending toward the Akamatsudani Valley on the southeastern flank due to the collapse of lobe 6-8. In May 1993, lobe 11 grew exogenously and block-and-ash flows started cascading into the Nakao River beyond the Taruki Height because the Oshigadani Valley had been filled with block-and-ash-flow deposits. Between 23 and 24 June 1993, northeastern part of lobe 11 largely collapsed in several times and block-and-ash flows ran down the Oshigadani Valley, sweeping the Senbongi District. Lobe 11 continued to grow exogenously by October 1993 and became the largest lobe in this eruption.

After November 1993, the style of dome growth changed from exogenous to endogenous, although lobe 12 and 13 appeared in January and July 1994, respectively. The dome swelled and uplifted because of the intrusion of the lava within the dome. Local deformations of the dome resulted in collapse of lava blocks and generated small block-and-ash flows. In October 1994, the extrusion of a lava spine started at the top of the endogenous dome. No block-and-ash flows were generated from the spine (Ui et al., 1999). The supply of magma to the dome stopped in late March 1995 and the end of eruption was officially declared on 25 May 1995.

2.2 Lava domes

Fugen-dake volcano is capped by the lava dome and their fragmented lava blocks, which was newly named Heisei-Shinzan (Fig. 2). The dimensions of the lava dome are 1.2 km long, 0.8 km wide, and 230-540 m thick (Nakada et al., 1999). The dome consists of thirteen lava lobes, which grew exogenously, and lavas which intruded within the dome (endogenous growth). The exogenous growth occurred when the effusion rate of the lava was high, while the endogenous growth occurred when the effusion rate was low (Nakada et al., 1995).

The western part of the dome is covered with abundant large lava blocks of several meters in diameter, which supplied during the endogenous growth in the final stage. The lava blocks are polygonal with flat sur-

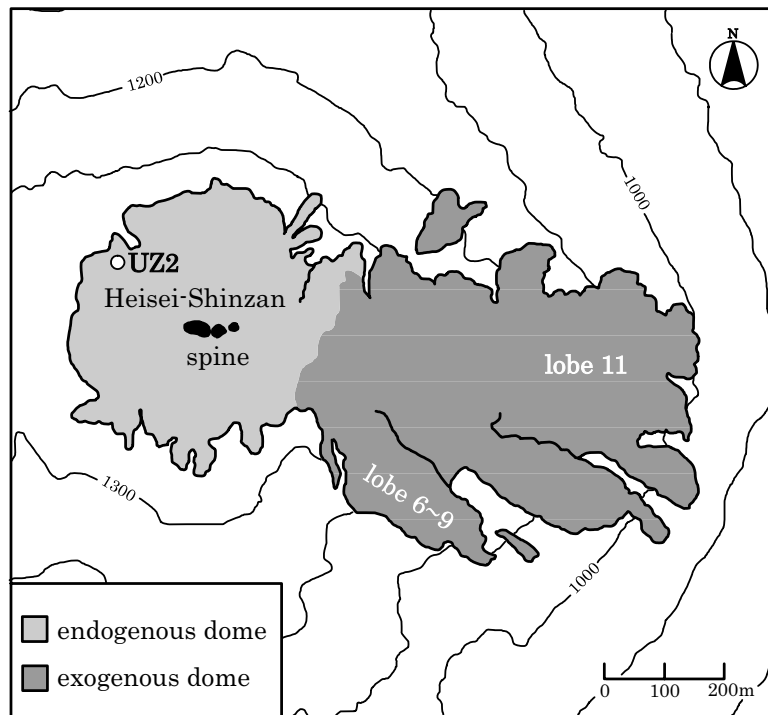


Fig. 2 Simplified map of the lava dome. One sampling location (UZ2) is shown.

face, which suffered oxidation and became reddish. Some blocks are partly devitrified and the matrix became bright-grayish. Warm volcanic gas is still on between some blocks, especially around the spine (Fig. 3a). There is a large lava block on the northwestern edge of the summit surface, in which an optical prism for electric-optical distance measurements was installed (Fig. 3b). The size of the block is about 9m width and 7m height. The surface of the block is partly devitrified. The northern surface of the block is highly oxidized and well vesiculated (Fig. 3c). The oxidized surface is about 30 cm thick. Large jigsaw cracks open in the center of the block (Fig. 3d). The lava around the cracks is not oxidized.

The exogenous dome is mainly emplaced on the eastern slope of Fugen-dake volcano (Fig. 2). Present surface of the eastern dome is mostly covered with lobe 11, which is the largest lobe in this eruption. The exogenous dome collapsed frequently and generated many block-and-ash flows toward the east. Access to the exogenous dome is very difficult and dangerous because the eastern slope of the dome is steep and the flow front of the lobe prevents us from approaching. In the western part of the dome, there is a lava spine, whose blocky

surface is difficult to walk, and some fumaroles.

2.3 Block-and-ash-flow deposits

Block-and-ash-flow deposits are distributed around the dome, especially along the four river valleys, the Mizunashi and the Nakao River, the Oshigadani and the Akamatsudani Valley (Fig. 1). Ash-cloud surge deposits are spread over the marginal areas of the block-and-ash-flow deposits and debris-flow deposits are emplaced in the lower reach of the rivers (Miyabuchi, 1999).

Block-and-ash-flow deposits are composed of dense dacite lava blocks and a fine-grained unconsolidated ash matrix of the same lithology. Juvenile dacite lava blocks are dark gray in color and poorly vesiculated. They are porphyritic and contain phenocrysts of plagioclase, hornblende, biotite, quartz, iron-titanium oxides and pyroxene. The sizes of the lava blocks range from a few centimeters to over 10 m. Some blocks are devitrified or oxidized to varying degrees. Block-and-ash-flow deposits consist of several flow units at most outcrops. Flow units are gray to red in color and include much fine-grained ash matrix. Each unit is separated by fine ash layers and some are reversely graded. In some units,

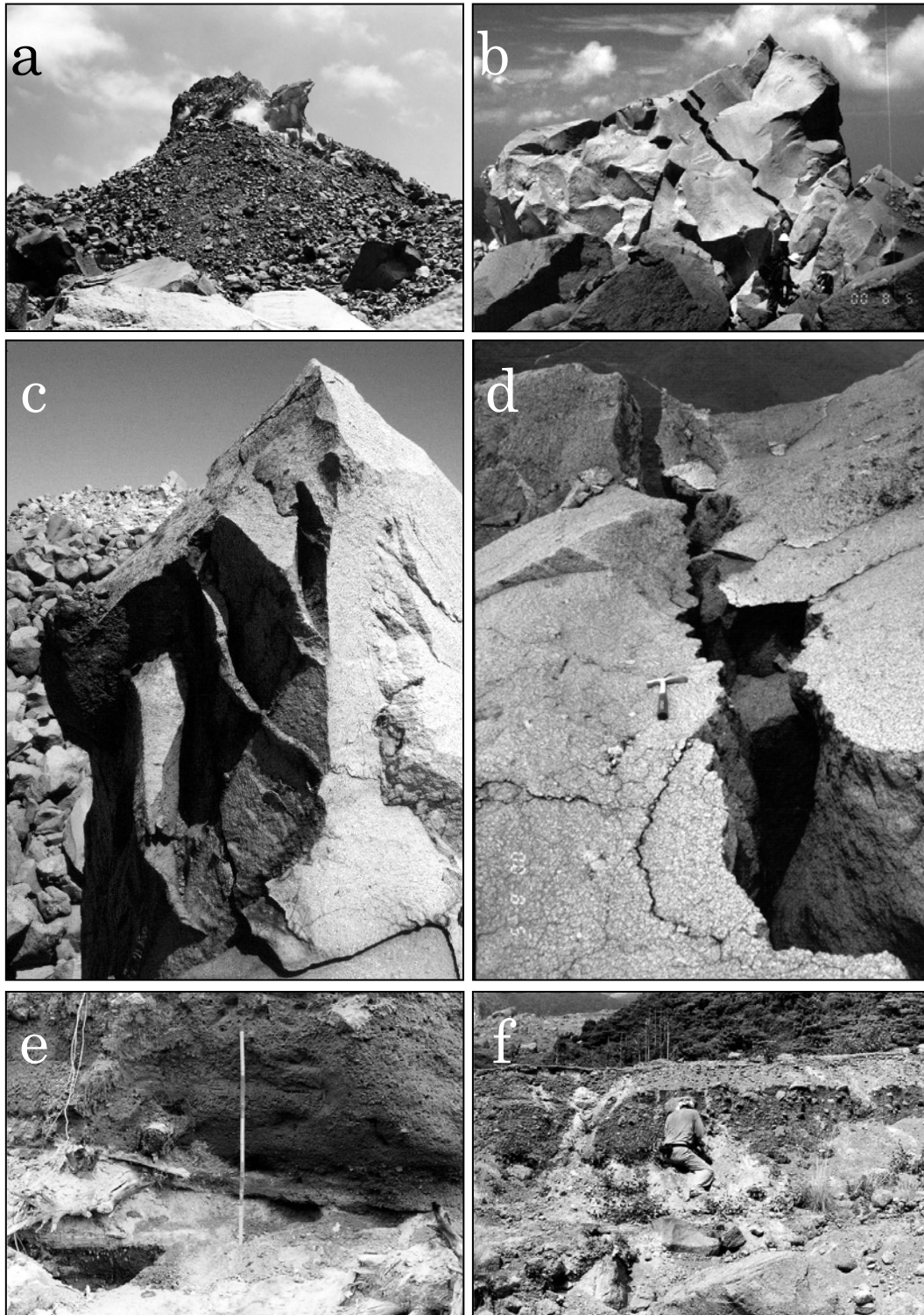


Fig. 3 Photographs of Unzen volcano and sampling site. (a) Western side of lava spine at the summit of Unzen volcano. Thick piles of fragmented lava blocks became talus. (b) A large lava block on the northwestern edge of the summit surface (UZ2). (c) The oxidized surface of the block, from which five samples (UZ201-205) were taken. (d) The large jigsaw cracks opened in the center of the block, from which five samples (UZ206-210) were taken. (e) The block-and-ash-flow deposits in the Senbongi District (UZ1). A large carbonized wood fragment is contained at the left side of the scale. (f) The block-and-ash-flow deposits at a confluence of the Mizunashi River and the Oshigadani Valley (UZ5).

carbonized wood fragments are contained and segregation pipes developed at the top of the unit (Fig. 3e). Debris-flow deposits are also emplaced at most outcrops. They are fines-depleted and cross stratifications developed in some units.

3. Sampling

Lava blocks were sampled from the endogenous dome and block-and-ash-flow deposits of the 1990-1995 eruptions in August 2000. We tried to collect lava blocks oxidized to varying degrees from the lava domes with different growth styles. However, we could not get samples from exogenous dome. Therefore, we collected from block-and-ash-flow deposits originated from exogenous dome.

Twenty lava samples (UZ201-220) from the endogenous dome were collected from a large lava block with an optical prism (UZ2 in Fig. 2). Five samples (UZ201-205) were taken from reddish surface (Fig. 3c) and five (UZ206-210) were taken from the jigsaw cracks (Fig. 3d). The other ten (UZ211-220) samples were collected from massive body. Samples from block-and-ash-flow deposits were taken at three outcrops. At one outcrop in the Senbongi District (UZ1 in Fig. 1), fifteen samples (UZ101-115) were collected from the 24 June 1993 flows generated from lobe 11 (Fig. 3e). We also collected seventeen samples (UZ401-407,

UZ501-510) at a confluence of the Mizunashi River and the Oshigadani Valley (UZ5 in Fig. 1; Fig. 3f) and at the Akamatsudani Valley (UZ4 in Fig. 1) for comparison.

4. Classification of rock samples

First of all, we classified our rock samples into three types, based upon the macroscopic observation of rocks and upon the contribution of the magnetic minerals with high coercivity to the remanence, which was estimated from magnetic behaviors during progressive alternating-field demagnetization (PAFD) of natural remanent magnetization (NRM). This is because the information is relatively easy to obtain and is effective in judging magnetic properties and oxidation states, according to the studies of Yufu volcano, Japan (Saito et al., 2000; Saito et al., 2003; Saito et al., 2004).

In the laboratory, we prepared specimens of 25 mm diameter and 22 mm height cut from the sampled blocks. NRM of each specimen was measured using a spinner magnetometer (Natsuhara-Giken SMM-85). PAFD was carried out up to a peak alternating of 100 mT using a three-axis tumbler system (2G Enterprises) in a magnetic-shielded room at Kyoto University. The residual magnetic field in this room is less than 1 μ T around the measurement instruments.

Samples, whose NRM were almost completely demagnetized up to 100 mT, were classed as type A

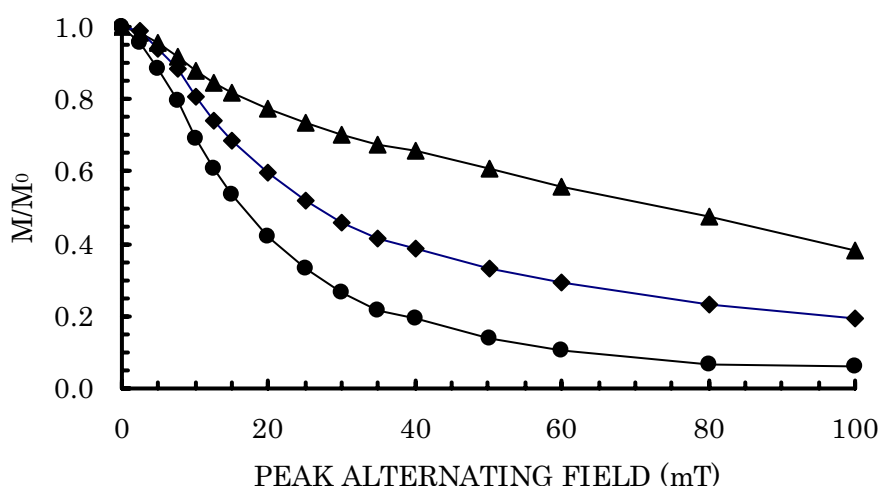


Fig. 4 Typical normalized PAFD curves of NRM. Circles, diamonds, and triangles denote an example of type A (UZ212), type B (UZ215), and type C (UZ101), respectively.

Table 1 Magnetic properties of Unzen samples.

	REMANENCE (Am^2/kg)			MDF (mT)		IRM (T)	SUS (m^3/kg)	COLOR
	NRM	ARM	SIRM	ARM	SIRM			
UZ101	4.32E-04		2.39E-02		70	1.5	9.30E-07	red
UZ102	7.02E-04	8.61E-04	3.58E-02	15	6.5	0.1	9.09E-06	dark grey
UZ103	9.68E-04	8.86E-04	5.68E-02	24	12.5	0.16	6.95E-06	white grey
UZ107	1.04E-03		6.04E-02		16	0.3	3.96E-06	white grey
UZ109	2.23E-03		5.91E-02		30	1.3	2.07E-06	red
UZ111	4.31E-03		7.88E-02		25	1.1	1.90E-06	red
UZ201	6.14E-04		2.60E-02		10	0.7	4.52E-06	partly red
UZ203	5.89E-04		2.46E-02		8	0.4	5.35E-06	partly red
UZ205	5.48E-04	4.70E-04	2.69E-02	20	8.5	0.25	5.86E-06	partly red
UZ210	7.25E-04	5.63E-04	4.18E-02	15	11	0.14	7.04E-06	white grey
UZ211	2.87E-04	4.76E-04	4.86E-02	13	10	0.14	6.55E-06	pink
UZ212	4.33E-04	4.67E-04	4.31E-02	13	9	0.14	6.75E-06	pink
UZ215	7.57E-04		4.75E-02		11	0.25	5.63E-06	pink
UZ219	1.34E-03		3.83E-02		19	0.9	2.44E-06	red
UZ401	2.39E-04	4.47E-04	2.71E-02	11	6	0.1	8.41E-06	white grey
UZ403	1.97E-04	4.48E-04	2.63E-02	10	7	0.1	6.83E-06	white grey
UZ404	4.41E-03		9.44E-02		29	0.9	2.55E-06	red
UZ405	5.35E-03	3.82E-03	1.22E-01	24	12	0.14	8.45E-06	dark grey
UZ501	4.63E-03		6.04E-02		26	1.5	1.50E-06	red
UZ503	7.54E-04		5.18E-02		11	0.2	5.11E-06	partly red
UZ506	3.26E-04	5.27E-04	2.39E-02	10	6	0.1	8.01E-06	dark grey
UZ510	1.12E-03	1.15E-03	6.56E-02	21	12.5	0.16	6.30E-06	white grey

Magnetic parameters: NRM = initial natural remanence; ARM = anhysteretic remanence; SIRM = saturation remanence; MDF = median destructive field; IRM 95% = the field in which the sample acquires 95% of SIRM; SUS = initial susceptibility.

(circles in Fig. 4). Lava blocks of type A are grayish or light grayish in color. Grayish blocks are glassy and light grayish blocks are crystalline, sometimes devitrified.

Samples, whose NRM could not be demagnetized completely at 100 mT and about 40% of initial NRM remained, were classed as type C (triangles in Fig. 4). Lava blocks of type C are reddish or dark reddish in color and contain weathered phenocrysts, especially broken down hornblende.

Samples which showed intermediate properties between type A and type C were classed as type B. The demagnetized curves of type B samples lay between the curves of type A and type C (diamonds in Fig. 4). Almost 20% of initial NRM still remained after demagnetized at 100 mT. Some lava blocks of type B have reticular reddish part in grayish groundmass. Some are uniformly oxidized and pink in color.

Samples from block-and-ash-flow deposits contained all three types, while samples from endogenous dome lacked glassy lava block.

5. Magnetic properties

In order to clarify the magnetic properties of Unzen samples, three kinds of rock magnetic experiments were conducted for selected samples from Unzen volcano. They were: (1) acquisition of isothermal remanent magnetization (IRM), (2) progressive thermal demagnetization (PThD) of the orthogonal IRM (Lowrie, 1990), and (3) the modified Lowrie-Fuller test (Johnson et al., 1975). By the first and second experiments, we can specify magnetic mineralogy in the samples. By the last experiment, we can specify the grain sizes of magnetite (titanomagnetite), if the magnetic minerals consist of magnetite only. We selected 22 representative samples for the experiments. All the experiments were conducted in a non-shielded room at Kyoto University. Measured magnetic parameters are shown in Table 1.

5.1 Acquisition of IRM

IRM was given with a pulse magnetizer (2G Enterprises MMPM-10) up to maximum fields of 1.7 T.

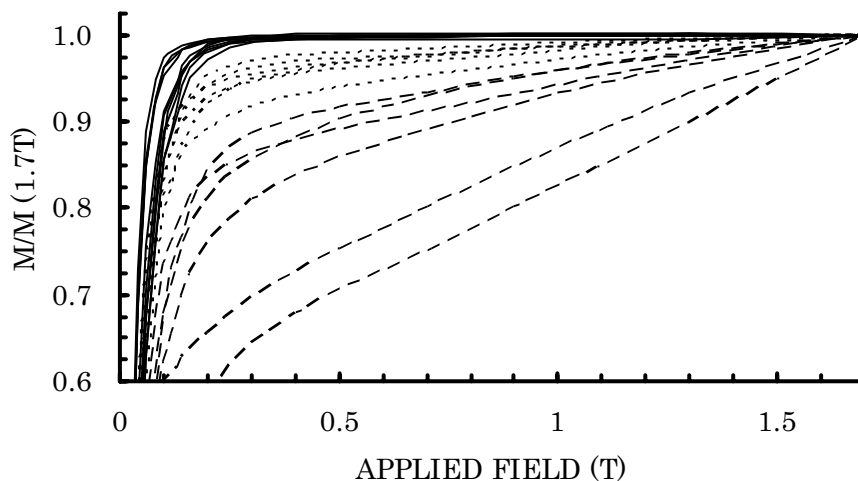


Fig. 5 Normalized IRM acquisition curves for Unzen samples in fields of up to 1.7 T. Solid, dotted, and broken lines denote type A, type B, and type C samples, respectively.

Before the acquisition, samples were demagnetized in an alternating field of 100 mT using a Natsuhara-Giken AF demagnetizer (DEM-8601M) with a three-axis tumbler system. Results are shown in Fig. 5. The normalized IRM acquisition curves for type A samples rose very steeply initially and reached over 95% by 0.1-0.16 T. Complete saturation was achieved by 0.3 T. The curves for type C samples rose steeply at first, but continued to climb and did not reach saturation even in 1.7 T, indicating the existence of magnetic minerals with high coercivity. The curves for type B samples lay between the curves of type A samples and type C samples.

5.2 Demagnetization of the orthogonal IRM

The orthogonal IRM was produced by applying a direct field of 1.7 T along the z -axis, followed by 0.4 T along the y -axis and finally 0.12 T along the x -axis. Then, PThD was carried out up to 580°C or 680°C in air using an electric furnace in a three-layer μ -metal magnetic shield. The residual field is less than 7 nT in the furnace. Low-field magnetic susceptibility of each specimen was measured using a Bartington MS2 magnetic susceptibility meter at each thermal demagnetization step for monitoring thermal alteration during PThD. As a result, the susceptibility change was less than 20% of the initial value and there is no abrupt change. Typical demagnetization results are shown in Fig. 6 by plotting and evaluating the thermal decay of each component separately.

The soft coercivity (< 0.12 T) fraction carried most of the IRM for type A samples and little magnetization

remained with the hard fraction (0.4-1.7 T; Fig. 6a and 6b). The soft fraction of most type A samples was demagnetized smoothly to zero at 540°C (Fig. 6b). This is strong evidence that titanomagnetite is the predominant and the only magnetic mineral. Some samples showed a large reduction at 400°C (Fig. 6a), indicating another titanomagnetite with different titanium content.

On the other hand, each fraction of type B and type C samples showed distinct unblocking temperatures (Fig. 6c and 6d). The soft fraction was demagnetized smoothly to zero up to 580°C, indicating the existence of titanomagnetite. The hard fraction abruptly dropped between 200°C and 250°C and was finally demagnetized at 680°C, indicating the existence of both titanohematite with intermediate composition and hematite.

Compared between samples, the medium fraction of type B and type C samples made a larger contribution to the remanence than that of type A. The hard fraction of type C made a larger contribution to the remanence than that of type B. The drop at 250°C of type C samples was larger than that of type B. These imply that magnetic carriers with high coercivity in type C samples made larger contribution than that in type A and type B.

5.3 The modified Lowrie-Fuller test

The modified Lowrie-Fuller test was conducted for type A samples because type B and type C samples contain magnetic minerals with high coercivity together with titanomagnetite. Anhysteretic remanent magnetization (ARM) was produced by applying a direct field of

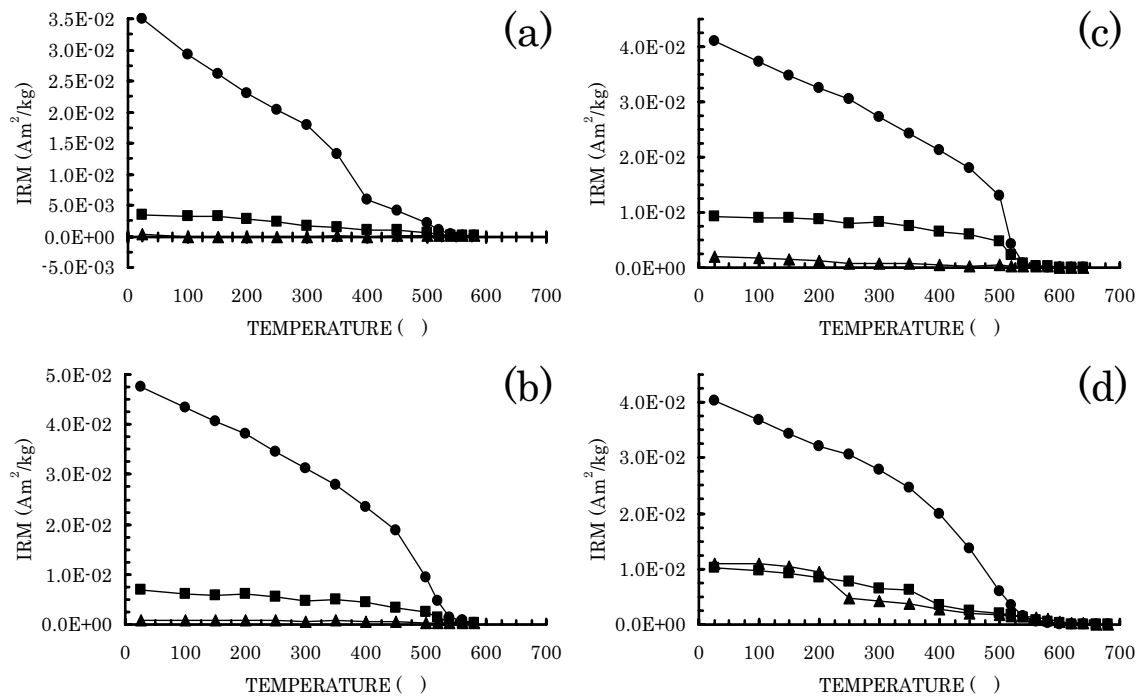


Fig. 6 Typical PThd results of the orthogonal IRM. (a) and (b) are results of type A samples (UZ102 and UZ211). (c) is a type B sample (UZ215) and (d) is a type C sample (UZ109). The orthogonal IRM was produced by magnetizing the sample in 1.7 T along the z-axis (triangles), followed by 0.4 T along the y-axis (squares) and then 0.12 T along the x-axis (circles).

0.1 mT in a peak alternating field of 100 mT. Saturation isothermal remanence (SIRM) was imparted at 1.7 T. Before each acquisition, samples were demagnetized in an alternating field of 100 mT. Then, PAFD of each artificial remanence was carried out up to a peak alternating field of 100 mT. All results showed the same magnetic behavior. The normalized PAFD curves of ARM and SIRM showed an exponential shape and SIRM curve always lay below that of ARM (Fig. 7).

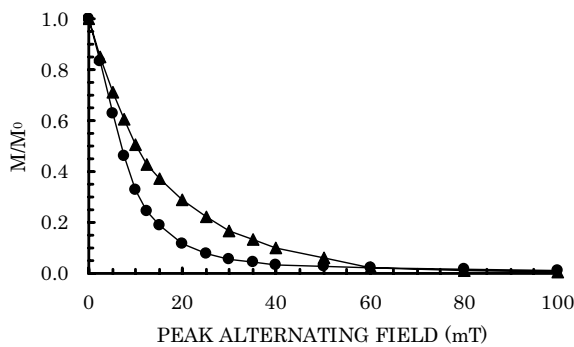


Fig. 7 Typical normalized PAFD curves of ARM (triangles) and SIRM (circles) for a type A sample (UZ403).

This is not a typical single-domain (SD) behavior or multidomain (MD) behavior. The results indicate strongly bimodal magnetite size distribution (Dunlop, 1983).

6. Oxide mineralogy

In order to characterize iron-titanium oxides in Unzen samples, we made optical microscope and electron microprobe analyses. Polished thin sections were prepared from our samples. These were examined by optical microscope in reflected light and by backscattered electron images using a JEOL JXA-8900 electron microprobe analyzer at Kobe University to identify occurrences, assemblages and textures of iron-titanium oxide minerals. Images of typical oxides are shown in Fig. 8. Based upon these observations, electron microprobe analyses of representative iron-titanium oxides were performed using the electron microprobe analyzer (Table 2). Analyses of iron-titanium oxides were recalculated on the basis of oxide stoichiometry to determine Fe_2O_3 and FeO from total Fe. Results of microprobe analyses are plotted on TiO_2 - FeO - $1/2\text{Fe}_2\text{O}_3$ ternary diagrams (Fig.

Table 2 Representative electron microprobe analyses (wt. %) of iron-titanium oxide minerals in Unzen samples.

	Type A						Type B					
	titanomagnetite			titanohematite			titanomagnetite			titanohematite		
	1	2	3	4	5	6	7	8	9	10	11	
MgO	1.25	1.22	2.26	1.97	2.42	2.04	0.97	1.01	1.27	1.20	0.58	
Al ₂ O ₃	1.60	1.37	5.13	0.93	0.22	0.14	2.24	2.56	2.33	0.58	1.13	
SiO ₂	0.04	0.05	0.21	0.00	0.06	0.03	0.04	0.03	0.11	0.05	0.09	
CaO	0.00	0.00	0.28	0.00	0.00	0.02	0.00	0.00	0.00	0.00	0.00	
TiO ₂	5.45	15.74	11.66	29.26	43.78	48.52	3.26	1.89	8.96	30.40	12.10	
Cr ₂ O ₃	0.04	0.12	0.04	0.05	0.03	0.00	0.14	0.16	0.11	0.21	0.13	
MnO	0.49	0.61	0.96	0.78	0.53	0.70	0.44	0.43	0.50	1.02	0.11	
FeO	85.44	76.28	73.69	64.31	51.56	47.30	86.75	87.44	81.41	62.25	77.88	
Total	94.31	95.38	94.27	97.30	98.63	98.75	93.83	93.52	94.69	95.71	92.02	
Fe ₂ O ₃	57.14	36.77	39.99	11.33	18.88	8.88	60.24	62.48	48.99	42.26	75.61	
FeO	34.02	43.19	37.71	54.11	34.58	39.31	32.55	31.22	37.33	24.22	9.84	
Total	100.03	99.07	98.27	98.44	100.52	99.64	99.87	99.77	99.60	99.95	99.60	
Mole fraction of Ti-rich comp	0.16	0.45	0.33	0.82	0.82	0.91	0.09	0.05	0.26	0.58	0.24	
	Type B				Type C							
	titanohematite				titanomagnetite		titanohematite			pseudobrookite		
	12	13	14	15	16	17	18	19	20	21	22	
MgO	3.17	3.89	2.42	0.05	4.97	0.75	0.53	2.34	0.04	1.73	2.19	
Al ₂ O ₃	0.23	0.47	0.19	0.04	6.67	2.51	1.44	0.23	1.04	0.22	0.59	
SiO ₂	0.01	0.00	0.02	0.09	0.03	0.04	0.14	0.00	0.02	0.02	0.00	
CaO	0.00	0.00	0.00	0.00	0.00	0.00	0.11	0.00	0.00	0.01	0.00	
TiO ₂	35.83	21.98	44.41	0.43	0.35	8.03	7.75	16.60	0.18	43.82	40.29	
Cr ₂ O ₃	0.01	0.02	0.02	0.00	0.11	0.10	0.12	0.00	0.00	0.03	0.00	
MnO	1.41	0.94	0.86	0.04	1.67	0.39	0.16	0.66	0.02	0.37	0.48	
FeO	56.31	66.84	50.03	88.68	79.86	83.07	80.13	72.29	88.14	49.23	50.87	
Total	96.96	94.14	97.94	89.37	93.67	94.89	90.37	92.16	89.44	95.44	94.41	
Fe ₂ O ₃	34.62	61.08	16.95	98.15	62.95	50.73	82.49	69.12	97.84	49.00	55.33	
FeO	25.15	11.87	34.78	0.36	23.22	37.43	5.90	10.09	0.10	5.13	1.08	
Total	100.42	100.26	99.64	99.21	99.97	99.98	98.63	99.09	99.24	100.35	99.95	
Mole fraction of Ti-rich comp	0.67	0.42	0.84	0.01	0.01	0.23	0.16	0.32	0.00	0.28	0.18	

Fe₂O₃ and FeO calculated on the basis of oxide stoichiometry. Mole fraction of Ti-rich component (Fe₂TiO₄ for titanomagnetite, FeTiO₃ for titanohematite and FeTi₂O₅ for pseudobrookite) is also shown. Analyses: 1, 2, large, homogeneous titanomagnetite; 3, small homogeneous titanomagnetite; 4, narrow titanomagnetite lamella in titanohematite; 5, 6, large homogeneous titanohematite; 7, 8, titanomagnetite separated by narrow titanohematite laths; 9, homogeneous titanomagnetite; 10, 11, titanohematite lamellas in titanomagnetite; 12, 13, titanohematite in which rutile lenses are developed; 14, homogeneous titanohematite; 15, small discrete hematite; 16, titanomagnetite separated by thick titanohematite laths; 17, homogeneous titanomagnetite; 18, titanohematite lamellas in titanomagnetite; 19, titanohematite in which rutile lenses are developed; 20, hematite; 21, 22, pseudobrookite.

9).

6.1 Type A

Iron-titanium oxides in type A samples are characterized by homogeneous titanomagnetite and titanohematite (Fig. 8a). Some titanomagnetite grains mantle with or attach to titanohematite. In some samples, narrow titanomagnetite lamellas along {0001} planes are ex-

solved in host titanohematite (Fig. 8b). Chemical compositions of homogenous titanomagnetite are within the

range $0.14 < x < 0.49$, mostly $0.15 < x < 0.25$, while titanohematite are within $0.76 < y < 0.96$ (Fig. 9a). Smaller titanomagnetite grains are within $0.18 < x < 0.47$

and more titaniferous than larger grains in most samples. Narrow lamellas in titanohematite are Ti-rich titanomagnetite with $0.44 < x < 0.97$.

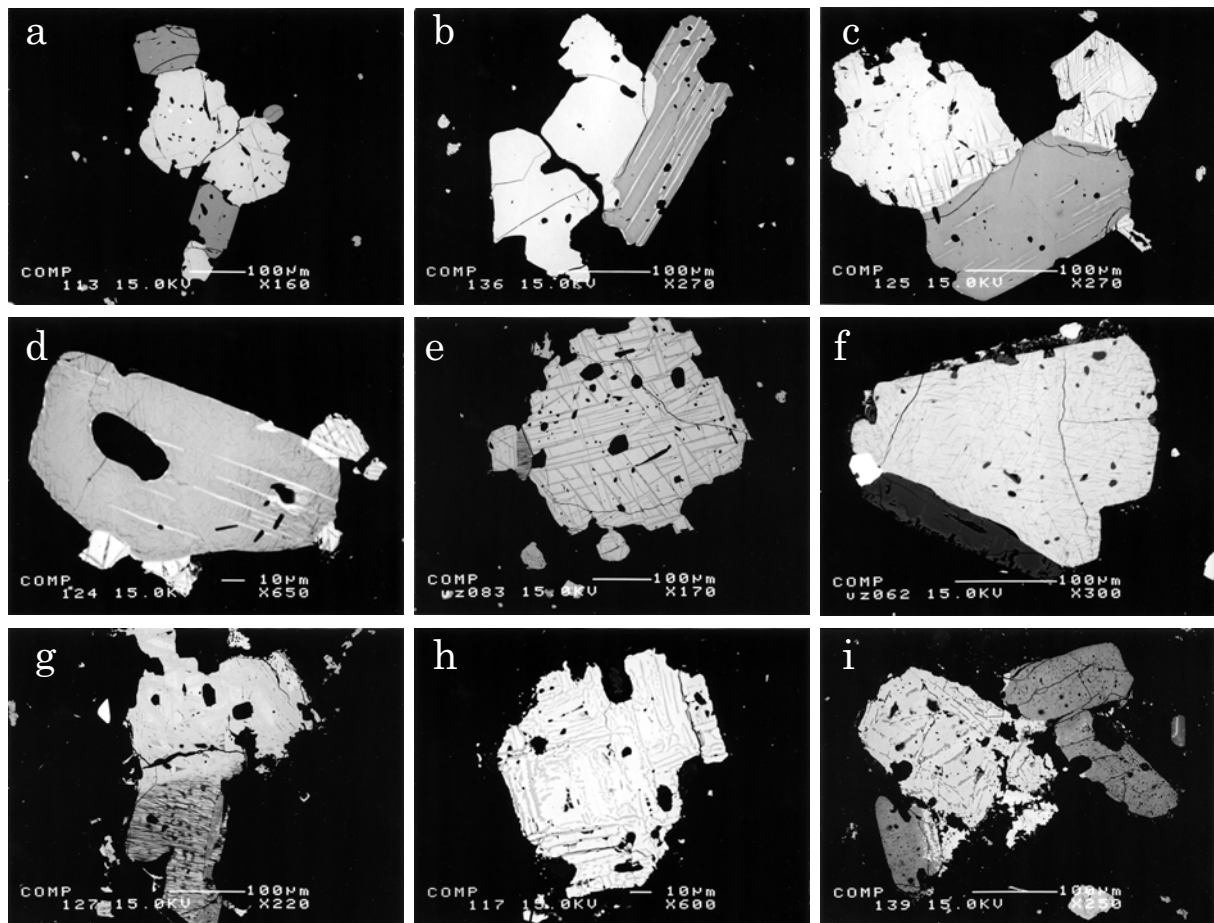


Fig. 8 Backscattered electron images of representative iron-titanium oxide minerals in Unzen samples. Image (a)-(b), (c)-(f), and (g)-(i) are in type A, type B, and type C samples, respectively. Refer to bar in lower center for scale. (a) Homogeneous titanomagnetite with titanohematite (darker) in UZ401. (b) Homogenous titanomagnetite and titanohematite with the oriented Ti-rich titanomagnetite lamellas along $\{0001\}$ planes in UZ510. (c) Weakly oxidized titanomagnetite and titanohematite in UZ215. Narrow titanohematite trellis lamellas are exsolved in host titanomagnetite. Ti-rich central core is lamella free. In host titanohematite, titanomagnetite lamellas are exsolved. (d) Weakly oxidized titanohematite in UZ215. The small z-shaped rutile lenses develop in host titanohematite, concentrating toward grain boundaries. Titanomagnetite lamellas are also exsolved. Note the white titanomagnetite lamellas cutting rutile lenses. (e) Trellis titanohematite lamellas develop uniformly in host titanomagnetite in UZ203. The z-shaped rutile lamellas (black) develop in the attached titanohematite. (f) The z-shaped rutile lenses develop uniformly in host titanohematite in UZ205. (g) Oxidized titanomagnetite (upper part) with thick trellis lamellas and titanohematite (lower part) with well developed rutile lamellas in UZ219. Pseudobrookite develops at the right end of primary titanohematite. (h) Strongly oxidized primary titanomagnetite in UZ404. Titanomagnetite is pseudomorphed by pseudobrookite along $\{111\}$ relic planes in a host of titanohematite. (i) Strongly oxidized primary titanomagnetite (central part) and titanohematite in UZ501. Primary titanomagnetite is pseudomorphed by pseudobrookite and titanohematite, like grain in image (h). Primary titanohematite is completely pseudomorphed by pseudobrookite (dark grey).

6.2 Type B

Iron-titanium oxides in type B samples are characterized by weakly exsolved grains with a small amount of lamellas. Large homogenous titanomagnetite and titanohematite are also present and their chemical compositions are within the range $0.14 < x < 0.44$ and $0.80 < y < 0.97$ (shown as open diamonds in Fig. 9b), almost the same composition as type A samples do.

In most titanomagnetite, especially in smaller grains, narrow trellis titanohematite lamellas are exsolved. In the grains with a smaller amount of lamellas, lamellas are concentrated along grain boundaries and central core of titanomagnetite is lamella free (Fig. 8c). In the grains with a larger amount of lamellas, trellis lamellas become thicker and distribute uniformly (Fig. 8e). The chemical composition of titanomagnetite without lamellas is in the same range ($0.16 < x < 0.18$) as homogenous grains. Titanium content of titanomagnetite decreases to 0.01 with increasing lamellas. The composition of titanohematite lamellas also becomes Ti-poor from 0.84 to about 0.2-0.1 with increasing lamellas. It is the reason for wide distribution of the chemical compositions of trellis type (shown as solid diamonds in Fig. 9b).

Titanohematite in type B is characterized by the exsolution of the z-shaped rutile lenses. Lenses develop along $\{0001\}$ and $\{0112\}$ planes of the titanohematite and concentrated along grain boundaries (Fig. 8d). With increasing lamellas, lenses become darker in color and distribute uniformly (Fig. 8e and 8f). The chemical composition of titanohematite becomes Ti-poor from 0.88 to 0.33 with increasing lamellas (shown as circles in Fig. 9b). In addition, white titanomagnetite lamellas are exsolved in some titanohematite. The lamellas cut rutile lenses, indicating the exsolution of titanomagnetite lamellas occurs after the exsolution of rutile lenses (Fig. 8d).

6.3 Type C

Iron-titanium oxides in type C samples are characterized by completely exsolved grains with pseudomorphed lamellas. Most titanomagnetite in type C samples is separated by abundant thick trellis lamellas of titanohematite (Fig. 8g). Titanohematite lamellas are homogeneous and there is no finer lamella within the lamellas. The composition of the titanomagnetite is very low x (below 0.05; shown as solid diamonds in Fig. 9c). It is nearly pure magnetite. Trellis lamellas are Ti-poor titanohematite with $0.10 < y < 0.33$ (shown as solid dia-

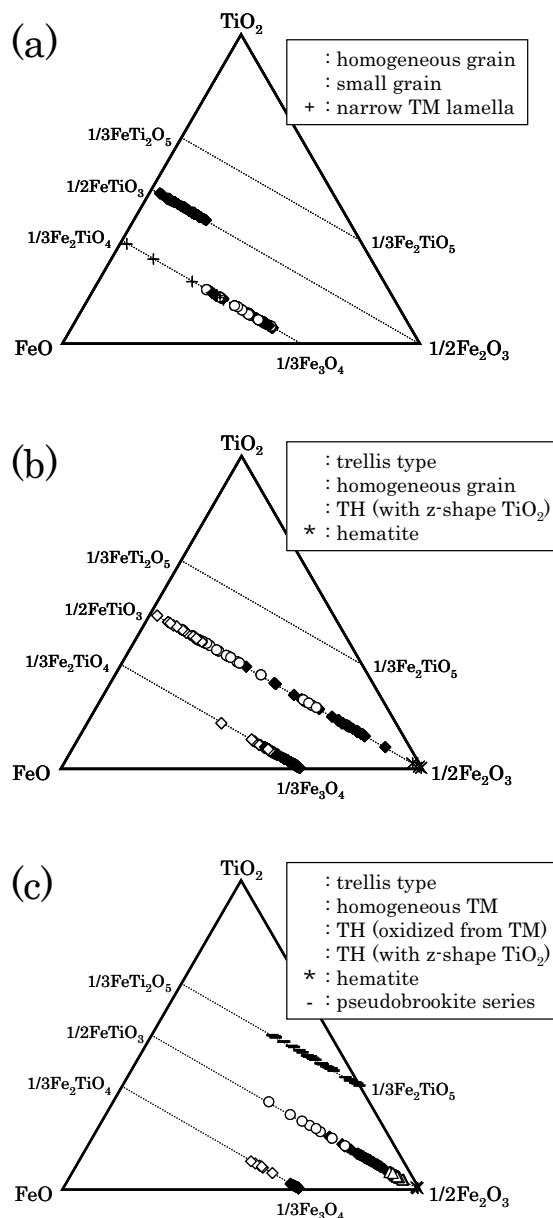


Fig. 9 TiO_2 - FeO - $1/2\text{Fe}_2\text{O}_3$ ternary diagrams showing compositions of iron-titanium oxide minerals in Unzen samples: (a) type A, (b) type B, and (c) type C samples. Minor components allocated as follows: $\text{FeO} = \Sigma\text{R}^{2+} = \text{Fe}^{2+} + \text{Mg} + \text{Mn} + \text{Ca}$; $\text{Fe}_2\text{O}_3 = 1/2\Sigma\text{R}^{3+} = 1/2(\text{Fe}^{3+} + \text{Al} + \text{Cr})$; $\text{TiO}_2 = \Sigma\text{R}^{4+} = \text{Ti} + \text{Si}$.

monds in Fig. 9c).

Titanohematite occurs with abundant thick z-shaped rutile lenses (Fig. 8g). Lenses are darker in color and thicker than that in type B. The composition of titanohematite is within the range $0.27 < y < 0.56$ (shown as circles in Fig. 9c). In some grains of this type, pseudobrookite is developed along grain boundaries (Fig. 8g).

Completely pseudomorphed grains are also existed (Fig. 8i).

Some pseudobrookite develops along relic {111} planes of primary titanomagnetite in a host of titanohematite (Fig. 8h and 8i). The chemical composition of this titanohematite is in the range $0.06 < y < 0.15$ (shown as triangles in Fig. 9c). The composition of pseudobrookite is within the range $z < 0.48$ (shown as bars in Fig. 9c). Hematite also occurs as discrete small grains. Its composition is $y < 0.01$ (shown as stars in Fig. 9c).

In addition, a few homogenous titanomagnetite grains are surprisingly existed in some samples. In such grains, there is no exsolution lamella. Its composition is within the range $0.15 < x < 0.27$ (shown as open diamonds in Fig. 9c), almost the same composition as type A samples do.

7. Discussion

7.1 Identification of iron-titanium oxide minerals

Rock magnetic analyses revealed the properties of magnetic iron-titanium oxide minerals and microscope and electron microprobe analyses identified all iron-titanium oxide minerals in Unzen samples.

Iron-titanium oxide minerals in type A samples are homogenous titanomagnetite with $0.14 < x < 0.49$ and titanohematite with $0.76 < y < 0.96$. The composition of titanomagnetite is consistent with rock magnetic results, although rock magnetic analyses cannot detect titanohematite with $y > 0.7$, which is not magnetic at and above room temperature. On the basis of the unblocking temperature distribution of the orthogonal IRM experiments, the estimated chemical composition of titanomagnetite is with $x \approx 0.1$ and 0.3 . Both values are within the range of microprobe results.

The determined compositions are also consistent with the values reported by three previous petrological works. Nakamura (1995) and Venezky and Rutherford (1999) analyzed the zoning profiles of iron-titanium oxides in Unzen samples and discussed the magma mixing. Nakamura (1995) reported that the chemical compositions of homogenous titanomagnetite and titanohematite are with $0.17 < x < 0.23$ and $0.79 < y < 0.82$, respectively. Venezky and Rutherford (1999) reported the chemical compositions of homogenous titanomagnetite and titanohematite are with $0.14 < x < 0.32$ and $0.73 < y < 0.78$, respectively. Nakada and Motomura (1999) studied petrology of Unzen samples and reported

that the chemical compositions of homogenous titanomagnetite and titanohematite are with $0.17 < x < 0.35$ and $0.79 < y < 0.83$, respectively. All values of previous works are within the range of our results. However, our values have much wider range than previous works. This may be because previous workers analyzed selected oxides in selected samples, which did not suffered oxidation, while we analyzed oxides, which suffered oxidation to various degrees, one after another.

In addition, Ti-rich titanomagnetite with $0.44 < x < 0.97$ is also identified in titanohematite grains. Rock magnetic analyses, however, do not indicate the existence of Ti-rich titanomagnetite. This may be because the amount of Ti-rich titanomagnetite is very low. As for the grain size of titanomagnetite, the modified Lowrie-Fuller test indicated not a typical SD or MD-type behavior, implying strongly bimodal size distribution (Dunlop, 1983).

Iron-titanium oxides in type B and type C samples are exsolved to various degrees. Rock magnetic results indicate the existence of hematite and titanohematite, together with titanomagnetite. The orthogonal IRM experiments suggest the composition of titanohematite is with $y \approx 0.5$. IRM acquisition suggests that type C samples include more magnetic minerals with high coercivity than type B samples (Fig. 5). Microprobe results are consistent with rock magnetic results described above. Microprobe analyses identified hematite with $y < 0.01$ and titanohematite with $y < 0.56$ in oxidized samples, together with titanomagnetite with $x < 0.05$. However, results for titanohematite are not completely consistent. Although rock magnetic analyses identified titanohematite with $y \approx 0.5$ only, microprobe analyses identified titanohematite with $y < 0.5$ besides hematite and titanohematite with $y \approx 0.5$ (Fig. 9b and 9c). The same inconsistency was also recognized in the Yufu results (Saito et al., 2004). It may be because either such titanohematite has a small saturation magnetization or the amount of such a mineral is lower than that of other minerals, although further rock magnetic analyses will be needed to identify such a mineral. In addition, pseudobrookite with $z < 0.48$ is commonly identified in type C samples although magnetic experiments cannot detect it.

7.2 Oxidation processes of iron-titanium oxides





Our results revealed that samples from Unzen volcano consist of three types with different iron-titanium oxide mineral assemblages. According to Saito et al.

(2004), it is suggested that the separation of samples are explained by deuteric oxidation of unoxidized oxides. On the basis of oxide mineral assemblages, we next discuss oxidation process of our lava samples.

Iron-titanium oxides in type A samples are characterized by homogeneous grains, while those in type B and type C samples are exsolved and composed of mul-

tiphase. According to the oxide classification by Haggerty (1991), type A oxides are classified as C1 and R1 stage, which is incipient and unoxidized stage. Oxides in type B samples are classified as C1-C3 and R1-R3 stage because titanomagnetite is separated by narrow trellis lamellas (Fig. 8e) and rutile lenses are well developed in titanohematite grains (Fig. 8f). Oxides in

Table 3 Reconstitution of typical iron-titanium oxides in type B and type C samples. (a) UZ203, (b) UZ404, (c) UZ201, (d) UZ210.

processed GIF image	color	composition	area ratio (%)	reconstituted composition
 <p>a</p>	grey	titanohematite ($y = 0.22$)	67	$\text{Fe}_{2.17}\text{Ti}_{0.16}\text{O}_{3.33}$
	light grey	titanomagnetite ($x = 0.03$)	33	
 <p>b</p>	grey	titanohematite ($y = 0.08$)	76	$\text{Fe}_{1.93}\text{Ti}_{0.31}\text{O}_{3.48}$
	black	pseudobrookite ($z = 0.05$)	24	
 <p>c</p>	grey	titanohematite ($y = 0.67$)	72	$\text{Fe}_{0.96}\text{Ti}_{0.76}\text{O}_{2.72}$
	black	rutile (TiO_2)	28	
 <p>d</p>	grey	titanohematite ($y = 0.84$)	95	$\text{Fe}_{1.21}\text{Ti}_{0.84}\text{O}_{3.05}$
	black	titanomagnetite ($x = 0.81$)	5	

type C samples are reached to C7 and R7 stage, which is the most strongly oxidized stage. Oxides in Fig. 8h and 8i are typical examples of stage C7 and R7. In the ternary diagrams, determined compositions of type C are distributed in the right side of the diagram, those of type A are distributed in the left and those of type B are intermediate between type A and type C (Fig. 9). In addition, magnetic results indicate that type B contains more hematite and Ti-poor titanohematite than type A does and type C contains much more than type B does (Fig. 5). These observations suggest that type B and type C oxides were produced from deuteritic oxidation of type A oxides (Saito et al., 2004).

In order to estimate oxidation process, we reconstituted typical composite grains and determined their chemical compositions before exsolution. Using digital image-editing software, we simplified photo images of oxides down to GIF images using only two colors. We obtained the area ratio of each phase in the grain from the histogram of brightness. We made a rough estimate of composition of the homogenized grain by multiplying

the area ratio by each chemical composition. The process is summarized in Table 3 and results are plotted on a ternary diagram (Fig. 10). Original compositions before reconstitution are plotted as squares and triangles tied with dashed lines and reconstituted compositions are indicated by stars.

Reconstituted compositions of oxides showing trellis titanohematite lamellas (Table 3a) and pseudobrookite lamellas (Table 3b) show almost the same Fe/Ti ratio as that of homogenous titanomagnetite (Fig. 10). This result indicates that homogenous titanomagnetite are oxidized to Ti-poor titanomagnetite with trellis titanohematite lamellas and to Ti-poor titanohematite with pseudobrookite lamellas by further oxidation. Reconstituted composition of titanohematite with z-shaped rutile lenses (Table 3c) shows almost the same Fe/Ti ratio as that of homogenous titanohematite and that of pseudobrookite in type C samples (Fig. 10). This result indicates that homogenous titanohematite is oxidized to titanohematite with rutile lenses and to pseudobrookite by further oxidation.

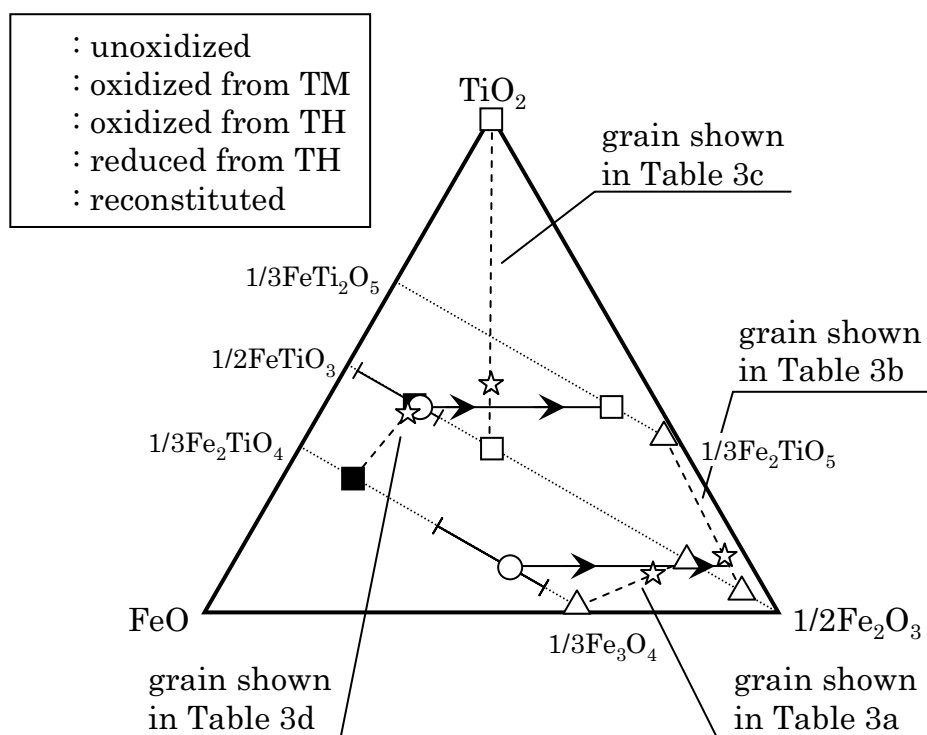


Fig. 10 Estimated oxidation and reduction processes plotted on a ternary diagram. Primary unoxidized titanomagnetite and titanohematite (circles) are oxidized along the arrows and transformed into complex grains: open squares are oxidized from primary titanohematite and triangles are oxidized from primary titanomagnetite. Solid squares are reduced from titanohematite. The composition range of the unoxidized oxides is also shown as bars. Stars are reconstituted compositions after Table 3.

In addition, reconstituted composition of titanohematite with titanomagnetite lamellas (Table 3d) shows almost the same Fe/Ti ratio as that of homogenous titanohematite and it is plotted on the left side of the line of titanohematite (Fig. 10). This result indicates that Ti-rich titanomagnetite are exsolved by reduction of homogenous titanohematite. The observation that titanomagnetite lamellas cut rutile lenses (Fig. 8d) indicates this reduction occurs after the deuteric oxidation. This type of grains is contained in type A and type B samples, while we cannot find in type C samples.

The oxidation and reduction processes are summarized as follows. (1) Primary homogenous titanomagnetite and titanohematite (type A) oxidized and titanohematite laths and rutile lenses are exsolved in host grains (type B). (2) By further oxidation, trellis lamellas are pseudomorphed by pseudobrookite and titanomagnetite are oxidized to Ti-poor titanohematite. Titanohematite with rutile lenses are completely pseudomorphed by pseudobrookite (type C). (3) After the oxidation, some oxides in type A and type B samples are reduced and Ti-rich titanomagnetite lamellas are exsolved in titanohematite grains.

7.3 Implications for lava dome oxidation processes

Our results revealed that deuteric oxidation resulted in three types of Unzen samples with different iron-titanium oxide mineral assemblages. Next, we discuss oxidation state and process in lava dome, based upon comparison between our samples.

Saito et al. (2004) found that lava blocks from the block-and-ash-flow deposits at Yufu volcano classified into two types with different iron-titanium oxide mineral assemblages. They clarified oxidation states and processes of samples on the basis of magnetic petrological analyses and suggested that oxidation occurred in lava dome. They also suggested that the different oxidation state is due to the difference of samples' positions in the lava dome or growth style of the dome. This is because oxidation is controlled by temperature, oxygen fugacity and retention time. In lava dome eruption, these parameters are thought to differ among the position in the dome, surface or interior, or the growth style, endogenous or exogenous. The exogenous dome generated much fresh lava due to successive supply of new lava, while the endogenous dome was exposed to the air for a long time at high temperature and oxidized because the hot lava intruded within the dome.

In this study, we verify that oxidation actually occurred in the lava dome and clarified the state and process in detail (Fig. 9 and 10). Samples from endogenous dome (UZ2) are oxidized to various degrees. Three among eight selected samples are unoxidized (type A), four are weakly oxidized (type B) and one is strongly oxidized (type C). Lava blocks sampled from surface are oxidized, while blocks from inner part are unoxidized. These results indicate that the position of the sample is the important factor in oxidation, as Saito et al. (2004) suggested.

Lava blocks from block-and-ash-flow deposits in exogenous dome origin (UZ1) are also oxidized to various degrees. Two among selected six samples are unoxidized (type A), one is weakly oxidized (type B) and three are strongly oxidized (type C). There is no definite difference of oxidation state and process between samples from endogenous dome and exogenous dome. Lava blocks from other block-and-ash-flow deposits (UZ4 and UZ5) also show various oxidation states. These results indicate that the degree of deuteric oxidation is not so different between endogenous and exogenous dome.

However, it does not indicate that endogenous dome and exogenous dome are oxidized to the same degrees by the same ways. Because this study aimed to analyze and verify the oxidation state and process in the lava dome, we selected samples oxidized to various degrees by design and did not pay attention to quantity or content ratio of oxidized blocks. Ui et al. (1999) reported that block-and-ash flows generated from the lava dome growing exogenously were derived from abundant fresh lava, while block-and-ash-flow deposits generated from the lava dome growing endogenously include lava blocks on the surface which had suffered various degrees of high temperature oxidation. Future study must aim to reveal the amount of oxidized zone in the lava dome and the content ratio of oxidized blocks to unoxidized blocks. Such a study may catch the difference of oxidation state and process between endogenous and exogenous dome.

In addition, two problems are newly identified. Some oxides in type A and type B samples showed the trace of reduction. However, reduction seems to be hard to occur in the lava dome, where abundant oxygen exists. Homogenous oxides in strongly oxidized type C samples are also hard to understand. We cannot interpret these problems at this time.

We conclude that deuteric oxidation actually occurred in Unzen lava dome and that oxidation state does

not differ between endogenous and exogenous dome. The position of the blocks in the lava dome, if anything, controls oxidation state; the surface of the dome is oxidized, while the inner part of the dome is unoxidized.

8. Conclusions

(1) Samples from the endogenous lava dome and the block-and-ash-flow deposits of the 1990-1995 eruption of Unzen volcano are classified into three types with different iron-titanium oxide mineral assemblages. Type A oxides are characterized by homogenous titanomagnetite and titanohematite. Type B oxides are weakly exsolved and titanohematite laths and rutile lenses develop. Type C oxides are completely exsolved and composed of multiphase; Ti-poor titanomagnetite, titanohematite, rutile and pseudobrookite. Some grains in type A and type B show the trace of reduction.

(2) The result of magnetic analyses is consistent with determined oxide mineralogy. In addition, magnetic analyses revealed that type C contains more magnetic minerals with high coercivity, hematite and Ti-poor titanohematite, than type B does.

(3) Chemical compositions measured by microprobe analyses show that oxides in type A samples are in a low oxidation state, while oxides in type C samples are in a high oxidation state and type B oxides are intermediate between type A and type C oxides. As the result of reconstitution of multiphase oxides, we found that type B and type C oxides are produced by oxidation of type A oxides.

(4) Samples from the surface of the endogenous dome are oxidized and those from the inner part of the dome are unoxidized. This indicates that the position of the sample is the important factor in oxidation. Samples from the block-and-ash-flow deposits in exogenous dome origin show almost the same oxidation state and process as those from endogenous dome do.

Acknowledgements

The electron microprobe analyses were done at Venture Business Laboratory of Kobe University. We would like to thank Dr. Naotaka Tomioka for helping with electron microprobe analyses.

References

- Dunlop, D.J. (1983): Determination of domain structure in igneous rocks by alternating field and other methods, *Earth Planet. Sci. Lett.* Vol. 63, pp. 353-367.
- Frost, B.R. (1991): Magnetic petrology: factors that control the occurrence of magnetite in crustal rocks. In: Lindsley, D.H. (Eds.), *Oxide Minerals: Petrologic and Magnetic Significance. Reviews in Mineralogy* 25, Mineralogical Society of America, pp. 489-509.
- Fujii, T. and Nakada, S. (1999): The 15 September 1991 pyroclastic flows at Unzen Volcano (Japan): a flow model for associated ash-cloud surges, *J. Volcanol. Geotherm. Res.* Vol. 89, pp. 159-172.
- Haggerty, S.E. (1991): Oxide textures - a mini-atlas. In: Lindsley, D.H. (Eds.), *Oxide Minerals: Petrologic and Magnetic Significance. Reviews in Mineralogy* 25, Mineralogical Society of America, pp. 303-321.
- Hoshizumi, H., Uto, K. and Watanabe, K. (1999): Geology and eruptive history of Unzen volcano, Shimabara Peninsula, Kyushu, SW Japan, *J. Volcanol. Geotherm. Res.* Vol. 89, pp. 81-94.
- Johnson, H.P., Lowrie, W. and Kent, D.V. (1975): Stability of anhysteretic remanent magnetization in fine and coarse magnetite and maghemite particles, *Geophys. J. R. Astron. Soc.* Vol. 41, pp. 1-10.
- La Croix, A. (1904): *La Montagne Pelee et ses eruptions*, Masson, Paris, 662 pp.
- Lowrie, W. (1990): Identification of ferromagnetic minerals in a rock by coercivity and unblocking temperature properties, *Geophys. Res. Lett.* Vol. 17, pp. 159-162.
- Matsumoto, Y. (1993): Conception of Beppu-Shimabara graben, its development and problems (in Japanese), *Mem. Geol. Soc. Jpn.* Vol. 41, pp. 175-192.
- Miyabuchi, Y. (1999): Deposits associated with the 1990-1995 eruption of Unzen volcano, Japan, *J. Volcanol. Geotherm. Res.* Vol. 89, pp. 139-158.
- Nakada, S. (2000): Hazards from pyroclastic flows and surges. In: Sigurdsson, H., Houghton, B.F., McNutt, S.R., Rymer, H., Stix, J., (Eds.), *Encyclopedia of Volcanoes. Academic press*, pp. 945-955.
- Nakada, S. and Fujii, T. (1993): Preliminary report on the activity at Unzen Volcano (Japan), November 1990-November 1991: dacite lava domes and pyroclastic flows, *J. Volcanol. Geotherm. Res.* Vol. 54, pp. 319-333.
- Nakada, S., Miyake, Y., Sato, H., Oshima, O. and Fuji-

- nawa, A. (1995): Endogenous growth of dacite dome at Unzen volcano (Japan), 1993-1994, *Geology* Vol. 23, pp. 157-160.
- Nakada, S. and Motomura, Y. (1999): Petrology of the 1991-1995 eruption at Unzen: effusion pulsation and groundmass crystallization, *J. Volcanol. Geotherm. Res.* Vol. 89, pp. 173-196.
- Nakada, S., Shimizu, H. and Ohta, K. (1999): Overview of the 1990-1995 eruption at Unzen Volcano, *J. Volcanol. Geotherm. Res.* Vol. 89, pp. 1-22.
- Nakamura, M. (1995): Continuous mixing of crystal mush and replenished magma in the ongoing Unzen eruption, *Geology* Vol. 23, pp. 807-810.
- Neumann van Padang, M. (1933): De uitbarsting van den Merapi (midden Java) in de jaren 1930-1931. *Ned. Indies, Dienst Mijnbouw. Vulkan. Seism. Mededel.*, 12.
- Newhall, C.G. and Melson, W.G. (1983): Explosive activity associated with the growth of volcanic domes, *J. Volcanol. Geotherm. Res.* Vol. 17, pp. 111-131.
- Ohta, K. (1973): A study of hot springs on the Shimabara Peninsula (in Japanese), *Sci. Rep. Shimabara Inst. Volcanol., Fac. Sci., Kyushu Univ.* Vol. 8, pp. 1-33.
- Saito, T., Kamata, H. and Ishikawa, N. (2000): Lithofacies and thermoremanent magnetism of the Ikeshiro pyroclastic-flow deposit and the Ikeshiro-Hokubu volcanoclastic deposit in Yufu-Tsurumi volcano group (in Japanese), *Bull. Volcanol. Soc. Jpn.* Vol. 45, pp. 217-224.
- Saito, T., Ishikawa, N. and Kamata, H. (2003): Identification of magnetic minerals carrying NRM in pyroclastic-flow deposits, *J. Volcanol. Geotherm. Res.* Vol. 126, pp. 127-142.
- Saito, T., Ishikawa, N. and Kamata, H. (2004): Iron-titanium oxide minerals in block-and-ash-flow deposits: implications for lava dome oxidation processes, *J. Volcanol. Geotherm. Res.* (in submitted).
- Sato, H., Fujii, T. and Nakada, S. (1992): Crumbling of dacite dome lava and generation of pyroclastic flows at Unzen Volcano. *Nature* Vol. 360, pp. 664-666.
- Stoiber, R.E. and Rose, W.I. Jr. (1969): Recent volcanic and fumarolic activity at Santiaguito volcano, Guatemala, *Bull. Volcanol.* Vol. 33, pp. 475-502.
- Ui, T., Matsuwo, N., Sumita, M. and Fujinawa, A. (1999): Generation of block and ash flows during the 1990-1995 eruption of Unzen Volcano, Japan, *J. Volcanol. Geotherm. Res.* Vol. 89, pp. 123-137.
- Venezky, D.Y. and Rutherford, M.J. (1999): Petrology and Fe-Ti oxide reequilibration of the 1991 Mount Unzen mixed magma, *J. Volcanol. Geotherm. Res.* Vol. 89, pp. 213-230.
- Wasilewski, P. and Warner, R.D. (1988): Magnetic petrology of deep crustal rocks - Ivrea Zone, Italy, *Earth Planet. Sci. Lett.* Vol. 87, pp. 347-361.

雲仙火山の磁気学的・岩石学的解析：溶岩ドーム内部の酸化過程

齋藤武士^{*}・石川尚人^{*}・鎌田浩毅^{*}

^{*} 京都大学 大学院人間・環境学研究科

要旨

溶岩ドーム内部の酸化状況・過程を明らかにするため、雲仙火山 1990-1995 年噴火の溶岩ドームと火砕流堆積物を対象に磁気学的・岩石学的解析を行った。その結果、ドームの表面の試料は強酸化されており、ドーム内部の試料は酸化されていないことが明らかになった。また、成長様式の異なる試料間の比較から、酸化状態は成長様式によらず、むしろドームでの位置の寄与の方が大きい可能性があることが明らかとなった。

キーワード：雲仙火山，溶岩ドーム，鉄チタン酸化物，岩石磁気，高温酸化現象